Enhanced Visible Light Photocatalysis of Bi2O3 Upon Fluorination

5 AUTHORS, INCLUDING:

Haiying Jiang
15 PUBLICATIONS   130 CITATIONS

SEE PROFILE

Kun Cheng
NED University of Engineering and Technolog…
3 PUBLICATIONS   86 CITATIONS

SEE PROFILE

Enhanced Visible Light Photocatalysis of Bi$_2$O$_3$ upon Fluorination

Hai-Ying Jiang, Jingjing Liu, Kun Cheng, Wenbin Sun, and Jun Lin*

Department of Chemistry, Renmin University of China, Beijing 100872, People's Republic of China

Ⓢ *Supporting Information*

ABSTRACT: For the better utilization of solar light and complete oxidation of environmental organic pollutants, it is desired to develop small band gap semiconductors with a deep valence band as efficient visible light photocatalysts. In this work, we prepared the fluorinated Bi$_2$O$_3$ catalysts using a precipitation method, followed by a solvothermal process in the presence of NH$_4$F. The fluorinated Bi$_2$O$_3$ catalysts, especially with the atomic ratio of F to Bi (R_F) at 0.2, exhibit much higher photocatalytic activities than the pure Bi$_2$O$_3$ for the degradation of methyl orange (MO) under the visible light irradiation. The effects of the fluorination on the phase structure, special surface areas, morphologies, optical properties, surface-adsorbed species, and electronic band structure of the Bi$_2$O$_3$ were investigated in detail. It was revealed that both the surface-adsorbed and lattice-substituted fluorine, induced by the fluorination to Bi$_2$O$_3$, play critical roles in the enhanced photocatalytic performance of the fluorinated Bi$_2$O$_3$. The two types of fluorine species effectively inhibit the recombination of the photoexcited electron−hole pairs by withdrawing the photoexcited electrons and increase the oxidation power of the photoexcited hole by lowering the valence band edge, respectively.
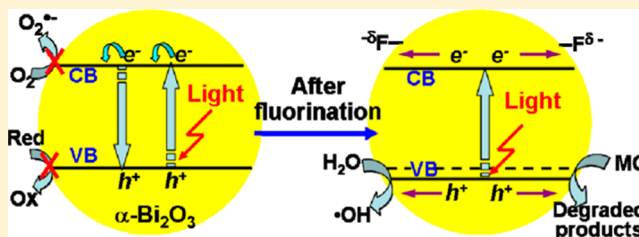
1. INTRODUCTION

Semiconductor photocatalysis with a primary focus on anatase TiO$_2$ has been extensively investigated as an efficient method for environmental pollution remediation and solar energy conversion.[1−3] However, its requirement of UV-irradiation activation seriously hinders the transition from basic research toward practical application. Therefore, many strategies have been proposed to develop visible light photocatalystic materials for the better utilization of solar light.[4−7] One noteworthy strategy is the development of the narrow band gap semiconductors as visible light photocatalystic materials.[8−11] Among the various narrow band gap semiconductors, bismuth oxide (Bi$_2$O$_3$) with band gap varying from 2.1 to 2.8 eV is a prospective candidate because of its unique characteristics including adequately high oxidation power of valence hole (∼+3.13 V vs NHE) and nontoxic property as TiO$_2$.[12−14] In the viewpoints of the efficient utilization of solar light, complete oxidation of environmental pollutants, and environmental friendly features, it is desired and meaningful to develop bismuth oxide (Bi$_2$O$_3$) as an efficient visible light photocatalystic material. However, pure Bi$_2$O$_3$ as a photocatalyst was found not to be as good as expected since its inability of the conduction band (CB) electron (∼+0.33 V vs NHE) to scavenge surface oxygen molecule ($E°$(O$_2$/O$_2^{•-}$) = −0.33 V vs NHE) results in a fast recombination of the photoexcited electron and hole. To solve this problem, a lot of works have been carried out, including the microstructure control and the surface deposition of noble metal.[15−18]

It was widely reported that the charge transfer against recombination can be effectively achieved by the fluorination of semiconductor photocatalysts.[19] Numerous works clearly demonstrated that the photocatalytic activity of semiconductor TiO$_2$ was significantly enhanced by surface fluorine modification or fluorine doping.[20−25] In addition, the improvement of photocatalytic activity was also observed over other fluorinated semiconductors such as SrTiO$_3$, ZnWO$_4$, and Bi$_2$WO$_6$.[26−28] According to these examples, we wonder if the fluorination would be also an effective way to enhance the photocatalytic performance of Bi$_2$O$_3$. To our best knowledge, as of now, the fluorinated Bi$_2$O$_3$ as a photocatalytic material has not been reported yet. Aiming at developing Bi$_2$O$_3$ as an efficient visible light photocatalyst, we prepared the fluorinated Bi$_2$O$_3$ with different atomic ratios of fluorine to bismuth by a facile approach in the present work. Upon visible light irradiation, the photocatalytic activity of Bi$_2$O$_3$ for the degradation of methyl orange (MO) has been shown to be remarkably enhanced after the fluorination. Furthermore, the role of the fluorination in the enhanced photocatalytic activity was revealed based on the results of various physicochemical characterizations and the analysis of the radical species formed in the visible light irradiated methanol suspension of pure Bi$_2$O$_3$ and fluorinated Bi$_2$O$_3$. This work evidences that the fluorination of semiconductor photocatalysts is a versatile method for improving the photocatalytic efficiencies of Bi$_2$O$_3$ and would be helpful for the development of the small band gap semiconductors with a deep valence band as efficient photocatalytic materials.

2. EXPERIMENTAL SECTION

2.1. Sample Preparation. All chemicals used in this study were analytic grade reagents without further purification. Fluorinated Bi_2O_3 samples were prepared using a precipitation method, followed by a solvothermal process. In detail, 10.78 g of $Bi(NO_3)_3 \cdot 5H_2O$ was dissolved in a 30 mL aqueous solution of HNO_3 (1.5 M). Under vigorous agitation, into the solution was NaOH solution (50% w/v) added dropwise until pH = 13, at which a yellow precipitate formed. Subsequently, the mixture was heated at 80 °C for 2 h, and then the resulting precipitate was collected by centrifugation and washed with deionized water and ethanol for several times before being dried at 100 °C for 12 h. Afterward, the freshly obtained precipitate (2.517 g) above was dispersed into a 20 mL mixed solution of ethanol−water (v/v = 9:1) containing the desired amount of $NH_4F \cdot H_2O$. The atomic ratios of F to Bi (R_F) in the dispersions are 0.0, 0.1, 0.2, and 0.3, respectively. The dispersion was then transferred to a Teflon-lined autoclave and treated at 150 °C for 4 h. After the reaction was completed, the yellow precipitate was recovered by centrifugation and washed with deionized water several times. Finally, the samples were calcined at 300 °C for 2 h to form the pure Bi_2O_3 ($R_F = 0$) and fluorinated Bi_2O_3 with different R_F values.

2.2. Characterization. X-ray diffraction (XRD) patterns of the as-prepared samples were recorded on an X-ray diffractometer (Shimadzu, XRD-7000) using Cu $K\alpha$ as X-ray radiation ($\lambda = 0.154\,18$ nm). The accelerating voltage and applied current are 40 kV and 30 mA, respectively. Fourier transform infrared (FTIR) spectra were obtained with an IRPrestige-21 FTIR spectrophotometer. The morphologies of these samples were observed by using a field-emission scanning electron microscope (FESEM) (JEOL JSM-7401E). The Brunauer−Emmett−Teller (BET) special surface areas were determined through nitrogen adsorption at 77 K using a Micromeritics Tristar 3020II instrument. X-ray photoelectron spectroscopy (XPS) and valence band X-ray photoelectron spectroscopy (VB XPS) were performed on an ESCALAB 250Xi spectrometer equipped with 300 W Al $K\alpha$ radiation. All binding energies were referenced to the C 1s peak (284.6 eV) of the surface adventitious carbon. The optical absorbance spectra of the samples were recorded on a UV−vis spectrophotometer (Hitachi U-3900) equipped with a diffuse reflectance accessory, and $BaSO_4$ was used as the reflectance standard.

2.3. Photocatalytic Activity Experiments. The degradation of methyl orange (MO) was carried out to evaluate the photocatalytic activities of the as-prepared pure Bi_2O_3 ($R_F = 0$) and fluorinated Bi_2O_3 with different R_F values. Typically, 10 mg sample was suspended in 100 mL aqueous solution of MO (4×10^{-5} M). The light source was a 300 W Xe arc lamp (CHF-XM150, Beijing Trusttech. Co. Ltd.) equipped with a wavelength cutoff filter for $\lambda > 420$ nm and positioned about 8 cm above the aqueous suspension. Prior to irradiation, the suspension was magnetically stirred in the dark for more than an hour to ensure the establishment of the equilibrium between the catalyst surface and MO molecules. At the given irradiation time intervals, 3 mL of the suspension was sampled, and then the catalyst and the MO solution were separated by centrifugation. The concentration of MO was determined by monitoring the change of the absorption spectrum in the absorbance at 461 nm with a Hitachi U-3310 spectrophotometer.

To study the photocatalytic oxidation pathway over these catalysts, triethanolamine (TEOA, 10 mM) as an effective hole scavenger and *tert*-butyl alcohol (TBA, 10 mM) as $^\bullet OH$ radicals scavenger (with a rate constant $k = 6 \times 10^8$) were chosen, respectively, to participate in the photocatalytic degradation of MO over these catalysts.[29] The determination of MO concentration during the photocatalytic reaction in the presence of TEOA or TBA was also conducted by measuring the absorption of MO solution at 461 nm.

2.4. ESR Measurement. To investigate the separation degree of the photoexcited electron−hole pairs over the as-prepared catalysts, the spin trap method was employed using diamagnetic DMPO to produce the stable paramagnetic spin-adduct with $^\bullet CH_2OH$ radicals formed in the visible light irradiated methanol suspensions of the catalysts. Prior to ESR measurement, the methanol suspension of the catalyst was bubbled with Ar gas for several minutes to remove the soluble oxygen. The DMPO−$^\bullet CH_2OH$ spin adduct was detected by an electron spin resonance spectrometer (ESR) (JEOL JES-FA 200) equipped with 500 Xe lamp as the irradiation source ($\lambda > 420$ nm). The settings for ESR spectrometer were centerfield = 323.17 mT, sweep width = 5 mT, microwave frequency = 9056 MHz, and microwave power = 7.99 mW.
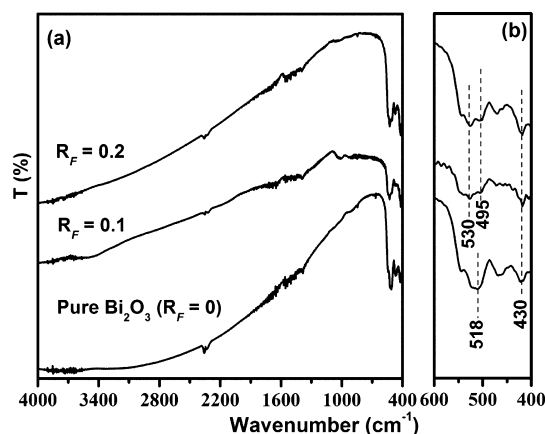
3. RESULTS AND DISCUSSION

3.1. Characterizations. XRD was used to indentify the phase structures and purities of the as-prepared samples. Figure 1a displays the XRD patterns of the pure Bi_2O_3 ($R_F = 0$) and
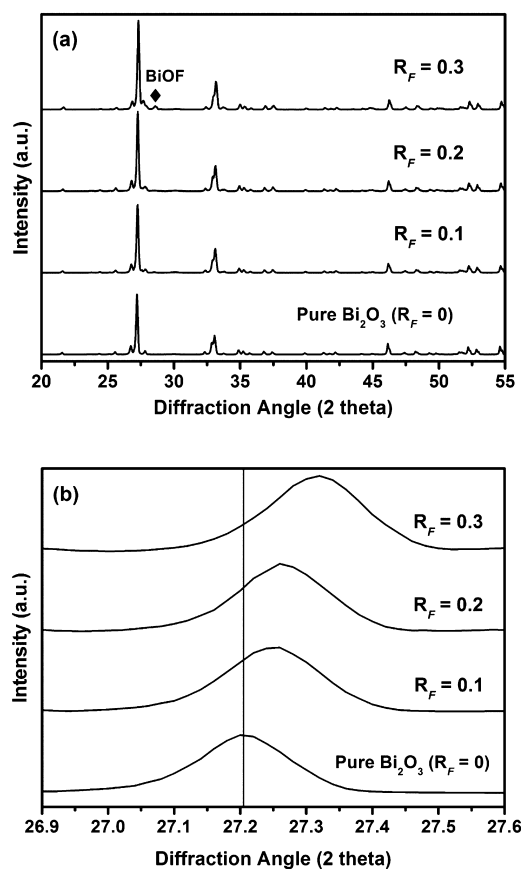
Figure 1. (a) X-ray diffraction patterns of pure Bi_2O_3 ($R_F = 0$) and fluorinated Bi_2O_3 with different R_F values. (b) Diffraction peak positions of the crystal plane (120) in the range of $2\theta = 26.9°−27.6°$.

fluorinated Bi_2O_3 with different R_F values. It is clearly observed that all samples exhibit a single monoclinic phase of well-crystalline α-Bi_2O_3 (JCPDS No. 41-1449) with an exception of the sample R_F = 0.3, in which minor impurity's diffraction peaks are found. The minor impurity could be indentified to be BiOF according to JCPDS file (No. 73-1595). Further observation indicates that with the increase in R_F value the XRD peak intensities of Bi_2O_3 phase slightly increase, and the widths of the XRD peaks appear to be sharper, indicating that the crystallization and crystal growth of the Bi_2O_3 are slightly enhanced. A similar phenomenon was also reported to occur on the fluorinated TiO_2,[21,30] probably caused by the mediating role of fluoride ions in the dissolution and recrystallization processes of metastable metal oxide intermediates.[19,31] A comparison of the (120) diffraction peaks of the pure Bi_2O_3 (R_F = 0) and fluorinated Bi_2O_3 with different R_F values in the range of 2θ = 26.9°−27.6° (see Figure 1b) shows that the (120) peak position obviously shifts toward a higher 2θ value with the increase of R_F value. Based on Bragg's law, the observed shift of the diffraction peaks to a higher angle directly reflects the lattice shrinkage of the detected crystals. The lattice shrinkage well suggests the substitution of the foreign F^- anion with smaller size (0.133 nm) for the host O^{2-} anion with larger size (0.14 nm) in the Bi_2O_3 host after the fluorination. Besides, the substitution of F^- anions for O^{2-} anions should cause the generation of Bi vacancies in the Bi_2O_3 host for charge compensation, which also contributes to the lattice shrinkage. The XRD results reveal that the fluorination on Bi_2O_3 in the present case not only introduces fluorine as substituting anion into the Bi_2O_3 host but also slightly improves the crystallinity of the Bi_2O_3.

Figure 2 shows the FT-IR spectra of the pure Bi_2O_3 (R_F = 0) and fluorinated Bi_2O_3 with different R_F values. It can be

peak at 518 cm^{-1} shifts to a higher wavenumber (530 cm^{-1}), accompanying an emergence of a new peak occurring at 495 cm^{-1}. Both the peaks show a trend of increase in strength with the increase of the R_F value. According to the related literature,[33] the peak at 495 cm^{-1} can be assigned to the stretching vibrations of Bi−F bonds. The location shift of the Bi−O bond stretching vibrations in the spectra of the fluorinated Bi_2O_3 probably originates from the change in the coordination environment surrounding Bi after the substitution of F^- for O^{2-} in the Bi_2O_3 host.

The BET surface areas of the pure Bi_2O_3 (R_F = 0) and fluorinated Bi_2O_3 with different R_F values are presented in Table 1. It can be seen that the surface area of the Bi_2O_3 is

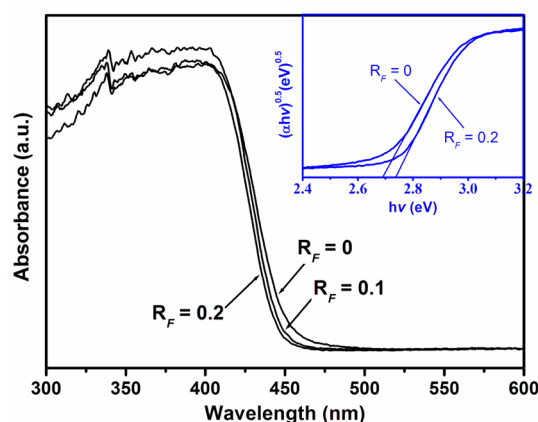**Table 1. BET Surface Areas of Fluorinated Bi_2O_3 with Different R_F Values**

R_F[a]	BET surf. area (m^2/g)	R_F[a]	BET surf. area (m^2/g)
0	0.392	0.2	0.659
0.1	0.802	0.3	0.692

[a]Atomic ratios of F to Bi.

apparently increased upon the fluorination, elucidating that the fluorination can largely inhibit the interconnection of sample particles. The FESEM observation (see Figure S1 in the Supporting Information) indicates that the fluorination on Bi_2O_3 (R_F = 0.2) has no obvious influences on the morphology and size. Both morphologies before and after fluorination appear to be microrod-shaped, which is similar to that of the α-Bi_2O_3 previously reported.[17,34]

The optical properties of the pure Bi_2O_3 (R_F = 0) and fluorinated Bi_2O_3 with different R_F values are revealed by the UV−vis diffuse reflectance spectra, as shown in Figure 3. It can
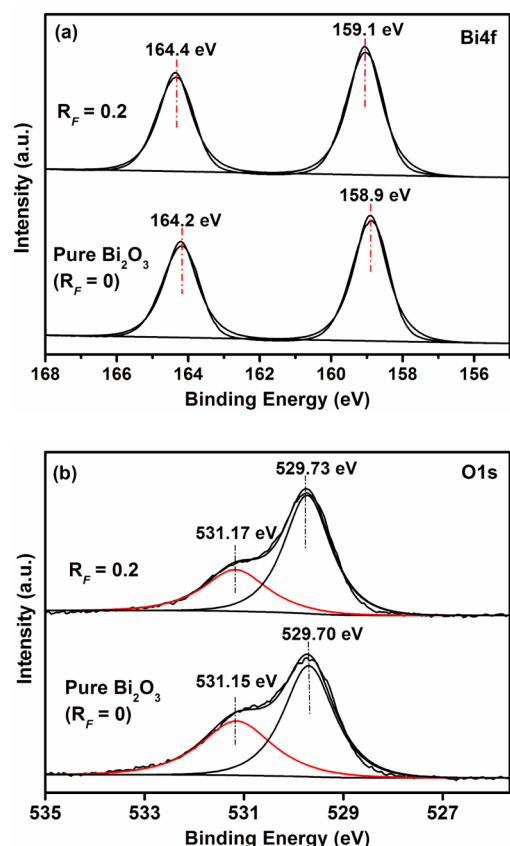

Figure 2. (a) FT-IR spectra of pure Bi_2O_3 (R_F = 0) and fluorinated Bi_2O_3 with different R_F values. (b) Enlarged FT-IR spectra in the region of 600−400 cm^{-1}.

Figure 3. UV−vis diffuse reflectance spectra of pure Bi_2O_3 (R_F = 0) and fluorinated Bi_2O_3 with different R_F values. The inset is the plot used to estimate the band gap value.

observed in Figure 2a that as compared to the fluorinated Bi_2O_3 samples, the pure Bi_2O_3 exhibits a broader band around 3450 cm^{-1}, which is associated with the stretching vibrations of hydrogen-bonded surface water molecules and hydroxyl groups. The enlarged FT-IR spectra in the region of 600−400 cm^{-1} is given in Figure 2b to clearly indentify the characteristic modes in these samples. In the spectrum of the pure Bi_2O_3 (R_F = 0), two peaks located at 518 and 430 cm^{-1} are ascribed to the stretching vibrations of Bi−O bonds of BiO_6 coordination polyhedron in α-Bi_2O_3 crystals.[32] After the fluorination, the

be seen that the fluorination obviously affects the light absorption characteristics of the Bi_2O_3. The pure Bi_2O_3 (R_F = 0) exhibits an intense absorption with the threshold at approximately 455 nm, which corresponds to the intrinsic band gap absorption of α-Bi_2O_3. The fluorination of the Bi_2O_3 leads to an obvious blue-shift in the absorption threshold, indicating an increase in the band gap. In the plots of $(\alpha h\nu)^{1/2}$ vs photo energy as shown in the inset of Figure 3, the band gaps of the pure Bi_2O_3 (R_F = 0) and fluorinated Bi_2O_3 (R_F =

0.2) are estimated from the tangent lines to be 2.68 and 2.74 eV, respectively.

To further explore the chemical states of the various elements in these samples, the pure Bi_2O_3 ($R_F = 0$) and fluorinated Bi_2O_3 ($R_F = 0.2$) were characterized by XPS analysis. Figure 4a presents the Bi 4f XPS spectra of the two

Figure 4. Bi 4f (a) and O 1s (b) XPS spectra of pure Bi_2O_3 ($R_F = 0$) and fluorinated Bi_2O_3 ($R_F = 0.2$).

samples. It can be observed that two peaks for the Bi 4f of the pure Bi_2O_3 are located at the binding energies of 158.9 and 164.2 eV, ascribed to Bi $4f_{7/2}$ and Bi $4f_{5/2}$, respectively, which is a characteristic of Bi^{3+} in α-Bi_2O_3.[17,35] However, the binding energies of Bi $4f_{7/2}$ and Bi $4f_{5/2}$ shift to 159.1 and 164.4 eV, respectively, after the fluorination in the case of the fluorinated Bi_2O_3 ($R_F = 0.2$). This observed shift to the higher binding energies clearly indicates the change in the chemical environment surrounding Bi and supports the replacement of O^{2-} by F^- with greater electronegativity, forming the mixed states such as F–Bi–O in the host lattice. The corresponding O 1s XPS profiles (Figure 4b) show that there are two surface oxygen species observed in both samples. The binding energy at the range of 529–530 eV is a characteristic of the lattice oxygen (O_L), whereas the binding energy of 531–532 eV could be attributed to the surface oxygen (O_S) present as hydroxyl group (–OH) bonded to surface.[36] On the basis of the relative XPS area, the atomic ratio of the surface oxygen (O_S) to the total oxygen ($O_S + O_L$) is dramatically decreased from 41% to 29% after the fluorination ($R_F = 0.2$). The decrease in the amount of the surface oxygen (O_S) would be due to the replacement of considerable surface groups (–OH) by –F species after the fluorination.

The high-resolution XPS spectrum of the F 1s region for the fluorinated Bi_2O_3 ($R_F = 0.2$) is given in Figure 5. As revealed in
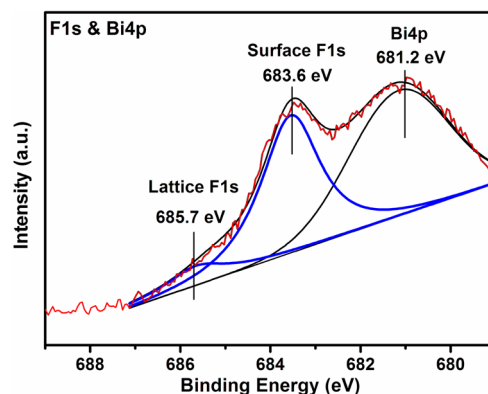
Figure 5. High-resolution XPS spectrum of the F 1s region for the fluorinated Bi_2O_3 ($R_F = 0.2$).

Figure 5, there are two types of fluorine species in the fluorinated Bi_2O_3 ($R_F = 0.2$). The peak at the binding energy of 683.6 eV can be assigned to the F species adsorbed on the host surface, while the peak at 685.7 eV is the F species substituting for O^{2-} in the host lattice.[37] Apparently, the F content on the host surface is much more than that in the host lattice. The existence of the surface and lattice fluorine species is well consistent with the XPS measurement results of the Bi 4f and O 1s species in the fluorinated Bi_2O_3 above.

The XPS measurements were also applied to determine the total density of states (DOS) distribution of the valence band (VB) for the pure Bi_2O_3 ($R_F = 0$) and fluorinated Bi_2O_3 ($R_F = 0.2$), as shown in Figure 6. It can be clearly seen that a slight
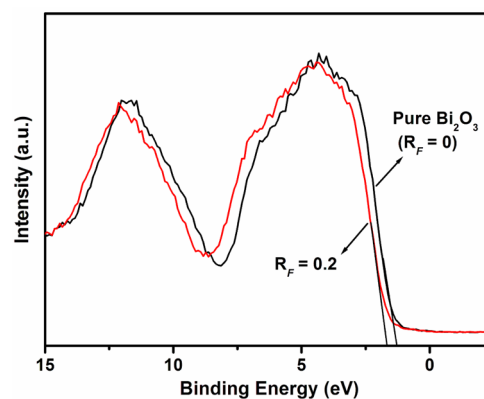

Figure 6. Valence band XPS spectra of pure Bi_2O_3 ($R_F = 0$) and fluorinated Bi_2O_3 ($R_F = 0.2$).

shift in the relative position of the valence band maximum (VBM) occurs after the fluorination. The VBM of the fluorinated Bi_2O_3 ($R_F = 0.2$) is approximately 0.06 eV more positive than that of the pure Bi_2O_3 ($R_F = 0$). The shift value is well comparable to the observed increase of the band gap from the diffuse reflectance spectra measurements (Figure 3), indicating the increase in the band gap of the fluorinated Bi_2O_3 ($R_F = 0.2$) originates from the lowering of its VBM. The VBM of Bi_2O_3 is composed of the hybrid of O 2p and Bi 6s orbitals.[12,38] The influences of the fluorination in the O and Bi (especially Bi) core levels, as evidenced by the XPS measurements, should be responsible for the lowering of the

20032

dx.doi.org/10.1021/jp406834d | J. Phys. Chem. C 2013, 117, 20029−20036

valence band maximum (VBM) of the fluorinated Bi_2O_3 (R_F = 0.2). The degradation of an organic pollutant over a photoirradiated semiconductor mainly refers to the behavior of the holes photoexcited on the valence band. The lowering of the valence band maximum (VBM) in the fluorinated Bi_2O_3 (R_F = 0.2) is possibly more helpful for the degradation of organic pollutants with respect to the oxidation power of the holes on the valence band.

3.2. Photocatalytic Properties. To investigate the effects of the fluorination on the photocatalytic properties of the Bi_2O_3, the photocatalytic activities for the degradation of MO over the pure Bi_2O_3 (R_F = 0) and fluorinated Bi_2O_3 with different R_F values were evaluated under the visible light irradiation (λ > 420 nm) for 120 min, as presented in Figure 7.
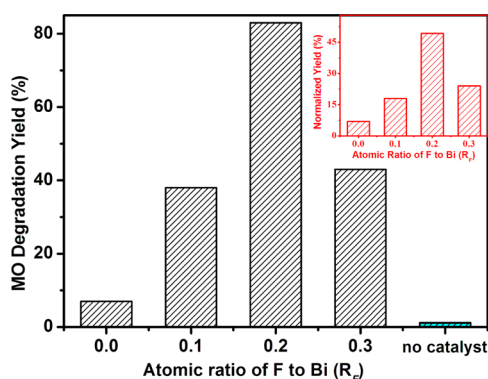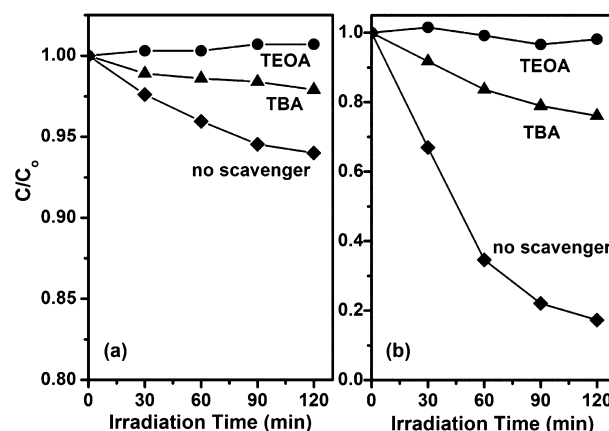

Figure 7. Photocatalytic degradation yield of MO over pure Bi_2O_3 (R_F = 0) and fluorinated Bi_2O_3 with different R_F values under visible light irradiation (λ > 420 nm) for 120 min. The inset is the normalized yield against R_F values. Normalized yield is obtained by multiplying the MO degradation yield by the surface area ratio of pure Bi_2O_3 (R_F = 0) to the corresponding catalyst.

The control experiment shows that the self-degradation of MO is negligible within the same irradiation time in the presence of no catalyst. The pure Bi_2O_3 (R_F = 0) exhibits a very poor photocatalytic activity. This is attributed to the inability of its CB electrons to scavenge the surface oxygen molecules, resulting in a fast recombination of the photoexcited electron and hole. All fluorinated Bi_2O_3 with different R_F values exhibit significantly higher activities than the pure Bi_2O_3 (R_F = 0), indicating that the fluorination is an efficient treatment method for enhancing the photocatalysis of Bi_2O_3. Furthermore, the activity of the fluorinated Bi_2O_3 strongly depends on the R_F value. With the increase of the R_F value, the activity reaches an optimum for the fluorinated Bi_2O_3 with R_F = 0.2, at which about 83% of MO was degraded under the irradiation for 2 h. After the optimum, the activity starts to drop when R_F = 0.3. Based on the above XRD results, there exists minor impurity of BiOF in the fluorinated Bi_2O_3 (R_F = 0.3). The conduction and valence band positions of BiOF are +1.97 and −1.73 vs NHE, respectively.[39] Therefore, its presence diminishes the quantum yield and active sites of the fluorinated Bi_2O_3 (R_F = 0.3), leading to a decrease in activity. It is well-known that the surface area of a catalyst could play an important role in its catalytic efficiency. As listed in Table 1, the surface area of the Bi_2O_3 is obviously increased after the fluorination. To ensure a fair evaluation of these photocatalysts' activities, the photocatalytic degradation rates of MO are normalized in term of the surface areas, as depicted in the inset of Figure 7. It can be found that the normalized activities of all fluorinated Bi_2O_3 are
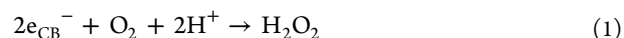
still much higher than that of the pure Bi_2O_3 (R_F = 0) and that the dependence of the activity on the R_F values is also the same as before the normalization.

Figure 8 presents the degradation of MO over the pure Bi_2O_3 (R_F = 0) and fluorinated Bi_2O_3 (R_F = 0.2) in the presence of

Figure 8. Photocatalytic degradation of MO over (a) pure Bi_2O_3 (R_F = 0) and (b) fluorinated Bi_2O_3 (R_F = 0.2) in the absence and presence of different scavengers under the visible light irradiation.
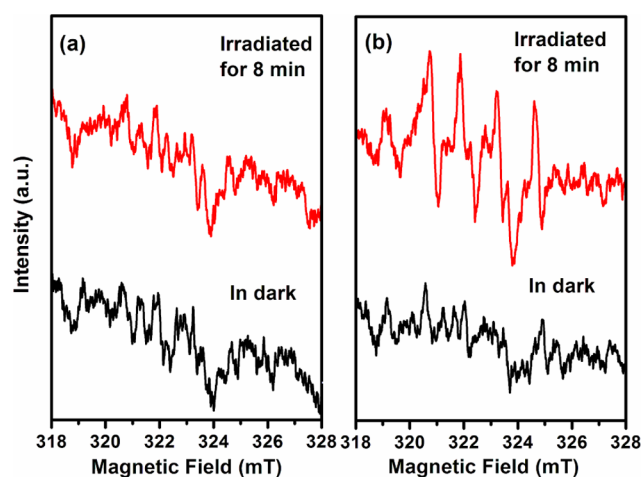
different scavengers upon the visible light irradiation (λ > 420 nm). As observed in Figure 8, over the two samples, the degradation efficiencies of MO are significantly reduced with the addition of $^\bullet OH$ scavenger TBA, and almost no MO degradation occurs when TEOA as an effective hole scavenger is added into the reaction solution. These results reveal that both $^\bullet OH$ radicals and photogenerated holes as active species are involved in the degradation of MO over the two samples, whereas $^\bullet OH$ radicals are major species in the photoreaction. Our previous studies found that the trace amount of the hydrogen peroxide (H_2O_2) could be produced over the irradiated Bi_2O_3 through the two-electron reduction process (reaction 1) in the presence of methanol as an electron donor.[17] With the excitation of the two catalysts by visible light irradiation, thus, there are two possible production paths of $^\bullet OH$ radicals in both systems. One is the reductive path of conduction band electron through reactions 1 and 2; the other is the oxidative path of valence band hole through reaction 3.

$$2e_{CB}^- + O_2 + 2H^+ \rightarrow H_2O_2 \tag{1}$$

$$H_2O_2 + e_{CB}^- \rightarrow OH^- + \bullet OH \tag{2}$$

$$h_{VB}^+ + H_2O\ (or-OH) \rightarrow \bullet OH \tag{3}$$

The disappearance of the MO degradation rate in the presence of TEOA infers that, in the two systems, reaction 3 is almost sole source of $^\bullet OH$ production, while the production of $^\bullet OH$ through reaction 2 is minor or negligible. In other words, the photoexcited hole not only directly degrades MO as active species but also acts as a sole production source of $^\bullet OH$ radical, as a result, intrinsically determining the final photocatalytic activity. The effective production yield of the photoexcited holes participating in both the degradation of MO and the reaction of $^\bullet OH$ production strongly depends on the separation degree of the photoexcited electron−hole pairs. According to the results shown in Figure 7, thus, it could be concluded that an efficient separation of the photoexcited electron−hole pair is
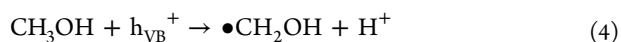
successfully achieved over the fluorinated Bi_2O_3, which results in the higher photocatalytic activities.

3.3. ESR Measurements and Understanding of Enhanced Photocatalysis over Fluorinated Bi_2O_3.

As evidenced by the characterization results above, two types of fluorine including the surface-adsorbed and lattice-substituted fluorine are induced onto or into the Bi_2O_3 after the fluorination. The surface-adsorbed fluorine, as formed by a simple ligand exchange between F^- and surface hydroxyl group $(-OH)$, is considered to play an important role in the separation of the photoexcited electron–hole pairs.[19] Since the electronegativity of F^- is much stronger than that of hydroxyl group $(-OH)$,[19,40] the surface-adsorbed F^- acting as an electron-trapping site can hold the trapped electron more tightly than the surface hydroxyl group $(-OH)$, as confirmed by the photocatalytic reduction reactivity of other fluorinated photocatalysts.[20] In other words, there is a stronger electron storage capacity on the surface of the fluorinated Bi_2O_3 than on that of the pure Bi_2O_3. The electron storage on the surface-adsorbed F^- retards the photoexcited electron transfer to the surface O_2, probably forming H_2O_2 through two-electron reduction process (reaction 1) in the present case,[17] but the recombination of the photoexcited electron–hole pair is effectively inhibited.[41] As a result, more photoexcited holes are allowed to react with surface H_2O (or $-OH$) to form more hydroxyl radicals or directly oxidize the organic compounds, giving a rise to the photocatalytic efficiency over the fluorinated Bi_2O_3. This understanding of the enhanced photocatalysis over the fluorinated Bi_2O_3 is well supported by the ESR spectra analysis of the $DMPO-{}^\bullet CH_2OH$ spin adduct formed in the visible light irradiated methanol suspensions of the pure Bi_2O_3 ($R_F = 0$) and fluorinated Bi_2O_3 ($R_F = 0.2$) in the absence of oxygen, shown in Figure 9. As reported earlier, in the present

evaluate the separation degree of the electron–hole pairs photoexcited over the pure Bi_2O_3 ($R_F = 0$) and fluorinated Bi_2O_3 ($R_F = 0.2$) in the presence of no any electron scavengers. It can be seen in Figure 9a,b that the characteristic ESR sextet peaks of a $DMPO-{}^\bullet CH_2OH$ spin adduct clearly appear over the fluorinated Bi_2O_3 ($R_F = 0.2$) after visible light irradiation for 8 min, while no such signals are apparently observed on both samples in the dark, even on the pure Bi_2O_3 ($R_F = 0$) within the same irradiation time. The generation of the apparent sextet peaks of $DMPO-{}^\bullet CH_2OH$ spin adducts well confirms that the electron storage capacity on the surface of the fluorinated Bi_2O_3 is much stronger than that of the pure Bi_2O_3, leading to an efficient separation of photoexcited electron–hole pairs. The ESR results also nicely parallels the results of the photocatalytic activities shown above. Meanwhile, the lowering of the valence band maximum (VBM) upon the substitution of F^- for O^{2-} in the Bi_2O_3 host after the fluorination, as evidenced by XRD and VB XPS measurements, equips the photoexcited hole with a more positive oxidation/reduction potential. From the viewpoint of the thermodynamics, such holes can more powerfully oxidize the organic compounds and react with the surface H_2O (or $-OH$) to form hydroxyl radical. Therefore, the lowering of the VBM, we believe, also substantially contributes to the generation of the apparent sextet peaks of $DMPO-{}^\bullet CH_2OH$ spin adducts (Figure 9) and the enhanced photocatalysis over the fluorinated Bi_2O_3 (Figure 7). The above understanding of the enhanced photocatalysis over the fluorinated Bi_2O_3 can be schematically illustrated in Scheme 1.

Scheme 1. Schematic Illustration of MO Photocatalytic Degradation over Fluorinated Bi_2O_3

Earlier investigations indicated the high degree of crystallinity facilitates the bulk diffusion of photogenerated charge carrier to the catalyst surface where photocatalytic reaction occurs.[45] Thus, we cannot rule out the possibility that the slight improvement in the crystallinity of Bi_2O_3 after the fluorination (see Figure 1) might be favorable for the photocatalysis of the fluorinated Bi_2O_3.

In summary, the fluorinated Bi_2O_3 has been synthesized through a precipitation method, followed by a solvethermal process. The fluorinated Bi_2O_3, especially with the atomic ratio of F to Bi at 0.2, exhibits a much higher photocatalytic activity than the pure Bi_2O_3 for the degradation of MO under the visible light irradiation. Both the surface-adsorbed and lattice-substituted fluorine in the fluorinated Bi_2O_3 play critical roles in the enhanced photocatalytic performance by inhibiting the recombination of the photoexcited electron–hole pair and increasing the oxidation power of the photoexcited hole. This work indicates that the fluorination is also a useful method for the development of the small band gap semiconductors with a deep valence band as efficient photocatalystic materials.

Figure 9. ESR signals of $DMPO-{}^\bullet CH_2OH$ spin adduct in (a) pure Bi_2O_3 ($R_F = 0$) and (b) fluorinated Bi_2O_3 ($R_F = 0.2$) methanol suspensions before and after visible light irradiation.
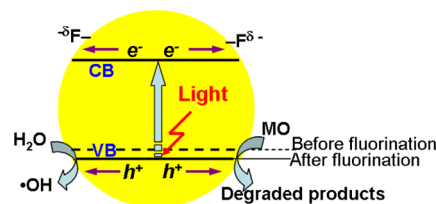
case, the photocatalytic oxidation of methanol by the photoexcited hole results in the formation of hydroxymethyl radicals through the reaction 4 only:[42,43]

$$CH_3OH + h_{VB}{}^+ \rightarrow {}^\bullet CH_2OH + H^+ \qquad (4)$$

The conversion of methanol to hydroxymethyl radicals proceeds rapidly with a rate constant, $k = 9.7 \times 10^8$ M^{-1} s^{-1}.[44] Herein, we attempted to detect the radical species to

Article

■ REFERENCES

(1) Linsebigler, A. L.; Lu, G. Q.; Yates, J. T. Photocatalysis on TiO_2 Surfaces: Principles, Mechanisms, and Selected Results. *Chem. Rev.* **1995**, *95*, 735−758.

(2) Chen, X.; Mao, S. S. Titanium Dioxide Nanomaterials: Synthesis, Properties, Modifications, and Applications. *Chem. Rev.* **2007**, *107*, 2891−2959.

(3) Ollis, D. F., Al-Ekabi, H., Eds.; *Photocatalytic Purification and Treatment of Water and Air*; Elsevier: Amsterdam, 1993.

(4) Asahi, R.; Morikawa, T.; Ohwaki, T.; Aoki, K.; Taga, Y. Visible-Light Photocatalysis in Nitrogen-Doped Titanium Oxides. *Science* **2001**, *293*, 269−271.

(5) Wang, D.; Kato, T.; Ye, J. Efficient Photocatalytic Decomposition of Acetaldehyde over a Solid-Solution Perovskite ($Ag_{0.75}Sr_{0.25}$)-($Nb_{0.75}Ti_{0.25}$)O_3 under Visible-Light Irradiation. *J. Am. Chem. Soc.* **2008**, *130*, 2724−2725.

(6) Li, H.; Bian, Z.; Zhu, J.; Huo, Y.; Li, H.; Lu, Y. Mesoporous Au/TiO_2 Nanocomposites with Enhanced Photocatalytic Activity. *J. Am. Chem. Soc.* **2007**, *129*, 4538−4539.

(7) Yu, J. C.; Wu, L.; Lin, J.; Li, P. S.; Li, Q. Microemulsion-Mediated Solvothermal Synthesis of Nanosized CdS-Sensitized TiO_2 Crystalline Photocatalyst. *Chem. Commun.* **2003**, *13*, 1552−1553.

(8) Zhao, Z.-G.; Miyauchi, M. Nanoporous-Walled Tungsten Oxide Nanotubes as Highly Active Visible-Light-Driven Photocatalysts. *Angew. Chem., Int. Ed.* **2008**, *47*, 7051−7055.

(9) Brezseinski, K.; Ostermann, R.; Hartmann, P.; Perlich, J.; Brezseinski, T. Exceptional Photocatalytic Activity of Ordered Mesoporous β-Bi_2O_3 Thin Films and Electrospun Nanofiber Mats. *Chem. Mater.* **2010**, *22*, 3079−3085.

(10) Kim, J.; Lee, C. W.; Choi, W. Platinized WO_3 as an Environmental Photocatalyst that Generates OH Radicals under Visible Light. *Environ. Sci. Technol.* **2010**, *44*, 6849−6854.

(11) Hirai, T.; Okubo, H.; Komasawa, I. Size-Selective Incorporation of CdS Nanoparticles into Mesoporous Silica. *J. Phys. Chem. B* **1999**, *103*, 4228−4230.

(12) Hameed, A.; Montini, T.; Gombac, V.; Fornasiero, P. Surface Phases and Photocatalytic Activity Correlation of Bi_2O_3/Bi_2O_{4-x} Nanocomposite. *J. Am. Chem. Soc.* **2008**, *130*, 9658−9689.

(13) Leontie, L.; Caraman, M.; Delibas, M.; Rusu, G. I. Optical Properties of Bismuth Trioxide Thin Films. *Mater. Res. Bull.* **2001**, *36*, 1629−1637.

(14) Bessekhouad, Y.; Robert, D.; Weber, J. V. Photocatalytic Activity of Cu_2O/TiO_2, Bi_2O_3/TiO_2 and $ZnMn_2O_4$/TiO_2 Heterojunctions. *Catal. Today* **2005**, *101*, 315−321.

(15) Zhou, L.; Wang, W.; Xu, H.; Sun, S.; Shang, M. Bi_2O_3 Hierarchical Nanostructures: Controllable Synthesis, Growth Mecha-

nism, and Their Application in Photocatalysis. *Chem.—Eur. J.* **2009**, *15*, 1776−1782.

(16) Hameed, A.; Gombac, V.; Montini, T.; Felisari, L.; Fornasiero, P. Photocatalytic Activity of Zinc Modified Bi_2O_3. *Phys. Chem. Lett.* **2009**, *483*, 254−261.

(17) Jiang, H.-Y.; Cheng, K.; Lin, J. Crystalline Metallic Au Nanoparticle-Loaded α-Bi_2O_3 Microrods for Improved Photocatalysis. *Phys. Chem. Chem. Phys.* **2012**, *14*, 12114−12121.

(18) Li, R.; Chen, W.; Kobayashi, H.; Ma, C. Platinum-Nanoparticle-Loaded Bismuth Oxide: an Efficient Plasmonic Photocatalyst Active under Visible Light. *Green Chem.* **2010**, *12*, 212−215.

(19) Liu, S.; Yu, J.; Cheng, B.; Jaroniec, M. Fluorinated Semiconductor Photocatalysts: Tunable Synthesis and Unique Properties. *Adv. Colloid Interface Sci.* **2012**, *173*, 35−53.

(20) Park, H.; Choi, W. Effects of TiO_2 Surface Fluorination on Photocatalytic Reactions and Photoelectrochemical Behaviors. *J. Phys. Chem. B* **2004**, *108*, 4086−4093.

(21) Yu, J. C.; Yu, J.; Ho, W.; Jiang, Z.; Zhang, L. Effects of F-Doping on the Photocatalytic Activity and Microstructures of Nanocrystalline TiO_2 Powders. *Chem. Mater.* **2002**, *14*, 3808−3816.

(22) Li, D.; Haneda, H.; Labhsetwar, N. K.; Hishita, S.; Ohashi, N. Visible-Light-Driven Photocatalysis on Fluorine-Doped TiO_2 Powders by the Creation of Surface Oxygen Vacancies. *Chem. Phys. Lett.* **2005**, *401*, 579−584.

(23) Xiang, Q.; Lv, K.; Yu, J. Pivotal Role of Fluorine in Enhanced Photocatalytic Activity of Anatase TiO_2 Nanosheets with Dominant (001) Facets for the Photocatalytic Degradation of Acetone in Air. *Appl. Catal. B: Environ.* **2010**, *96*, 557−564.

(24) Lv, K.; Cheng, B.; Yu, J.; Liu, G. Fluorine Ions-Mediated Morphology Control of Anatase TiO_2 with Enhanced Photocatalytic Activity. *Phys. Chem. Chem. Phys.* **2012**, *14*, 5349−5362.

(25) Yu, J.; Li, Q.; Liu, S.; Jaroniec, M. Ionic-Liquid-Assisted Synthesis of Uniform Fluorinated B/C-Codoped TiO_2 Nanocrystals and Their Enhanced Visible-Light Photocatalytic Activity. *Chem.—Eur. J.* **2013**, *19*, 2433−2441.

(26) Wang, J.; Yin, S.; Zhang, Q.; Satio, F.; Sato, T. Synthesis and Photocatalytic Activity of Fluorine Doped $SrTiO_3$. *J. Mater. Sci.* **2004**, *39*, 715−717.

(27) Huang, G.; Zhu, Y. Enhanced Photocatalytic Activity of $ZnWO_4$ Catalyst via Fluorine Doping. *J. Phys. Chem. C* **2007**, *111*, 11952−11958.

(28) Shi, R.; Huang, G.; Lin, J.; Zhu, Y. Photocatalytic Activity Enhancement for Bi_2WO_6 by Fluorine Substitution. *J. Phys. Chem. C* **2009**, *113*, 19633−19638.

(29) Buxton, G. V.; Greenstock, C. L.; Helman, W. P.; Ross, A. B. Critical Review of Rate Constants for Reactions of Hydrated Electrons, Hydrogen Atoms and Hydroxyl Radicals (•OH/•O⁻) in Aqueous Solution. *J. Phys. Chem. Ref. Data* **1988**, *17*, 513−886.

(30) Yu, J.; Wang, W.; Cheng, B.; Su, B.-L. Enhancement of Photocatalytic Activity of Mesporous TiO_2 Powders by Hydrothermal Surface Fluorination Treatment. *J. Phys. Chem. C* **2009**, *113*, 6743−6750.

(31) Yu, J.; Xiang, Q.; Ran, J.; Mann, S. One-Step Hydrothermal Fabrication and Photocatalytic Activity of Surface-Fluorinated TiO_2 Hollow Microspheres and Tabular Anatase Single Micro-Crystals with High-Energy Facets. *CrystEngComm* **2010**, *12*, 872−879.

(32) Ai, Z.; Huang, Y.; Lee, S.; Zhang, L. Monoclinic α-Bi_2O_3 Photocatalyst for Efficient Removal of Gaseous NO and HCHO under Visible Light Irradiation. *J. Alloys Compd.* **2011**, *509*, 2044−2049.

(33) Kavun, V. Y.; Merkulov, E. B.; Ignat'eva, L. N.; Goncharuk, V. K. Ionic Mobility and Structure of Glasses Based on Indium and Bismuth Fluorides from Data of IR and F-19 NMR Spectroscopy. *Glass Phys. Chem.* **2000**, *26*, 199−201.

(34) Muruganandham, M.; Amutha, R.; Lee, G.-H.; Hsieh, S.-H.; Wu, J.; Sillanpää, M. Facile Fabrication of Tunable Bi_2O_3 Self-Assembly and Its Visible Light Photocatalytic Activity. *J. Phys. Chem. C* **2012**, *116*, 12906−12915.

(35) Bian, Z.; Zhu, J.; Wang, S.; Cao, Y.; Qian, X.; Li, H. Self-Assembly of Active Bi_2O_3/TiO_2 Visible Photocatalyst with Ordered

Mesoporous Structure and Highly Crystallized Anatase. *J. Phys. Chem. C* **2008**, *112*, 6258−6262.

(36) Tang, X.; Li, Y.; Huang, X.; Xu, Y.; Zhu, H.; Wang, J.; Shen, W. MnO$_x$−CeO$_2$ Mixed Oxide Catalysts for Complete Oxidation of Formaldehyde: Effect of Preparation Method and Calcination Temperature. *Appl. Catal. B: Environ.* **2006**, *62*, 265−273.

(37) Hu, S.; Zhu, J.; Wu, L.; Wang, X.; Liu, P.; Zhang, Y.; Li, Z. Effect of Fluorination on Photocatalytic Degradation of Rhodamine B over In(OH)$_y$S$_z$: Promotion or Suppression? *J. Phys. Chem. C* **2011**, *115*, 460−467.

(38) Wu, J.; Huang, F.; Lu, X.; Chen, P. One-pot Synthesis of BiSbO$_4$ Nanophotocatalyst with Enhanced Visible-Light Performance. *CrystEngComm* **2011**, *13*, 3920−3924.

(39) Huang, W.; Zhu, Q. DFT Calculations on the Electronic Structures of BiOX (X = F, Cl, Br, I) Photocatalysts With and Without Semicore Bi 5d States. *J. Comput. Chem.* **2009**, *30*, 182−190.

(40) Yu, J. C.; Ho, W.; Yu, J.; Hark, S. K.; Lu, K. Effects of Trifluoroacetic Acid Modification on the Surface Microstructures and Photocatalytic Activity of Mesoporous TiO$_2$ Thin Films. *Langmuir* **2003**, *19*, 3889−3896.

(41) Monllor-Satoca, D.; Gomez, R. Electrochemical Method for Studying the Kinetics of Electron Recombination and Transfer Reactions in Heterogeneous Photocatalysis The Effect of Fluorination on TiO$_2$ Nanoporous Layers. *J. Phys. Chem. C* **2008**, *112*, 139−147.

(42) Di Iorio, Y.; Aguirre, M. E.; Brusa, M. A.; Grela, M. A. Surface Chemistry Determines Electron Storage Capabilities in Alcoholic Sols of Titanium Dioxide Nanoparticles. A Combined FTIR and Room Temperature EPR Investigation. *J. Phys. Chem. C* **2012**, *116*, 9646−9652.

(43) Kandiel, T. A.; Dillert, R.; Bahnemann, D. W. Enhanced Photocatalytic Production of Molecular Hydrogen on TiO$_2$ Modified with Pt−Polypyrrole Nanocomposites. *Photochem. Photobiol. Sci.* **2009**, *8*, 683−690.

(44) Ulanski, P.; Von Sonntag, C. The OH Radical-Induced Chain Reactions of Methanol with Hydrogen Peroxide and with Peroxodisulfate. *J. Chem. Soc., Perkin Trans.* **1999**, *2*, 165−168.

(45) Kong, M.; Li, Y.; Chen, X.; Tian, T.; Fang, P.; Zheng, F.; Zhao, X. Tuning the Relative Concentration Ratio of Bulk Defects to Surface Defects in TiO$_2$ Nanocrystals Leads to High Photocatalytic Efficiency. *J. Am. Chem. Soc.* **2011**, *133*, 16414−16417.